AFRL-DE-PS-
TP-2006-1020

Noise analysis for complex field estimation using a self-referencing interferometer wave front sensor (Postprint)

Troy Rhoadarmer
Jeffery D. Barchers

3 July 2002

Conference Proceeding

APPROVED FOR PUBLIC RELEASE; DISTRIBUTION IS UNLIMITED.

This work published in High-Resolution Wavefront Control: Methods, Devices, and Application IV, proceedings of SPIE, Vol. 4825, 2002.

AIR FORCE RESEARCH LABORATORY
Directed Energy Directorate
3550 Aberdeen Ave SE
AIR FORCE MATERIEL COMMAND
KIRTLAND AIR FORCE BASE, NM 87117-5776

REPORT DOCUMENTATION PAGE

Form Approved
OMB No. 0704-0188

1. REPORT DATE *(DD-MM-YYYY)*	2. REPORT TYPE	3. DATES COVERED *(From - To)*
3 July 2002	Conference Proceedings (Postprint)	1 Apr 02 - 30 Sep 06

4. TITLE AND SUBTITLE
Noise analysis for complex field estimation using a Self-referencing interferometer wave front sensor (Postprint)

5a. CONTRACT NUMBER
In House- 299962

5b. GRANT NUMBER

5c. PROGRAM ELEMENT NUMBER
063605F

6. AUTHOR(S)
Troy A. Rhoadarmer, Jeffery D. Barchers*

5d. PROJECT NUMBER
JT00

5e. TASK NUMBER
S0

5f. WORK UNIT NUMBER
AB

7. PERFORMING ORGANIZATION NAME(S) AND ADDRESS(ES)

AFRL/DES
3550 Aberdeen Ave. SE
Kirtland AFB, NM 87117-5776

*Science Applications International Corp

8. PERFORMING ORGANIZATION REPORT NUMBER

9. SPONSORING / MONITORING AGENCY NAME(S) AND ADDRESS(ES)
AIR FORCE RESEARCH LAB
3550 Aberdeen Ave SE
Kirtland AFB, NM 87117-5776

10. SPONSOR/MONITOR'S ACRONYM(S)
AFRL/DES

11. SPONSOR/MONITOR'S REPORT NUMBER(S)
AFRL-DE-PS-TP-2006-1020

12. DISTRIBUTION / AVAILABILITY STATEMENT

Approved for Public Release; Distribution is Unlimited.

13. SUPPLEMENTARY NOTES
This work published in High-Resolution Wavefront Control: Methods, Devices, and Application IV, proceedings of SPIE, Vol. 4825, pp. 215-227, 2002. One or more of the authors is a U.S. Government employee working within the scope of their position; therefore, the U.S. Government is joint owner of the work and has the right to copy, distribute, and use the work. Any other form of use is subject to copyright restrictions.

14. ABSTRACT
A noise analysis for complex field reconstruction from a self-referencing interferometer wave front sensor with an amplified reference is evaluated. The wave front sensor is constructed from a phase-shifting, point diffraction interferometer where the reference field is created by coupling a focal plane image of the input optical filed into a n optical amplifier. The noise characteristics of the wave front sensor are examined in terms of the field estimations Strehl. The effects of several systems parameters are examined- shot noise, read noise, quantization noise, the relative intensities of the signal and reference fields, spontaneous emission from the amplifier, and phase shift errors.

15. SUBJECT TERMS
Adaptive optics, interferometer, scintillation, wave front sensors

16. SECURITY CLASSIFICATION OF:			17. LIMITATION OF ABSTRACT	18. NUMBER OF PAGES	19a. NAME OF RESPONSIBLE PERSON
a. REPORT	b. ABSTRACT	c. THIS PAGE			Troy Rhoadarmer
Unclassified	Unclassified	Unclassified	SAR	15	19b. TELEPHONE NUMBER *(include area code)* N/A

Noise analysis for complex field estimation using a self-referencing interferometer wave front sensor

Troy A. Rhoadarmer

Starfire Optical Range, Directed Energy Directorate,
US Air Force Research Laboratory, Kirtland AFB, NM 87117-5776 USA

Jeffrey D. Barchers

Science Applications International Corporation,
Starfire Optical Range, Directed Energy Directorate,
US Air Force Research Laboratory, Kirtland AFB, NM 87117-5776 USA

ABSTRACT

A noise analysis is presented for complex field estimation using a self-referencing interferometer wave front sensor with an amplified reference. The wave front sensor is constructed from a phase-shifting, point diffraction interferometer. The reference field is created by coupling a part of the incident wave front into a single mode fiber where it is optically amplified. The noise characteristics of this wave front sensor are examined in terms of the field estimation Strehl. The effects of several system parameters are examined—shot noise, read noise, quantization noise, spontaneous emission from the amplifier, the relative intensities of the signal and reference fields, and temporal phase shifting.

Keywords: adaptive optics, interferometers, scintillation, wave front sensors

1. INTRODUCTION

Wave front sensing accuracy is a critical factor in determining the achievable Strehl ratio of an adaptive optical (AO) system. Many real-time AO systems in use today rely on either a Shack-Hartmann sensor or a shearing interferometer coupled with a least-squares reconstructor to form an estimate of the incident wave front.[1–5] Unfortunately, the performance of these systems degrades severely in strong scintillation due to the presence of branch points in the wave front phase and the effect of scintillation on the wave front sensor (WFS) measurements.[6–10] This reduction in estimation accuracy makes these WFS systems of limited use in applications which operate in strong, extended turbulence conditions. Even with a branch point reconstructor, designed to address the problems associated with scintillation, performance does not improve significantly.[11]

In this paper we describe a new WFS concept—the self-referencing interferometer (SRI) WFS with an amplified reference—that is being developed at the Air Force Research Laboratory, Directed Energy Directorate's Starfire Optical Range (SOR) and can be used with narrow-band, coherent light. Previous analysis has shown that, in the absence of noise, the wave front estimation accuracy of the SRI is immune to scintillation and is superior to either a Shack-Hartmann WFS or a shearing-interferometer WFS in strong scintillation.[9,10,12] A comparison of WFS performance based on wave optical simulations is shown in figure 1. In section 2 the analysis of the SRI is extended to consider the effects of noise on the accuracy of wave front estimation. Several sources of errors are considered—shot noise, read noise, quantization noise, spontaneous emission from the amplifier, the relative intensities of the signal and reference fields, and temporal phase shifting.

2. SELF-REFERENCING INTERFEROMETER WAVE FRONT SENSOR

The design and operation of the SRI WFS is described in this section along with an analysis of its noise properties. A laboratory demonstration of the SRI WFS is being developed at the SOR so the following discussion will be in the context of that application.

High-Resolution Wavefront Control: Methods, Devices, and Applications IV, John D. Gonglewski, Mikhail A. Vorontsov, Mark T. Gruneisen, Sergio R. Restaino, Robert K. Tyson, Editors, Proceedings of SPIE Vol. 4825 (2002) © 2002 SPIE · 0277-786X/02/$15.00

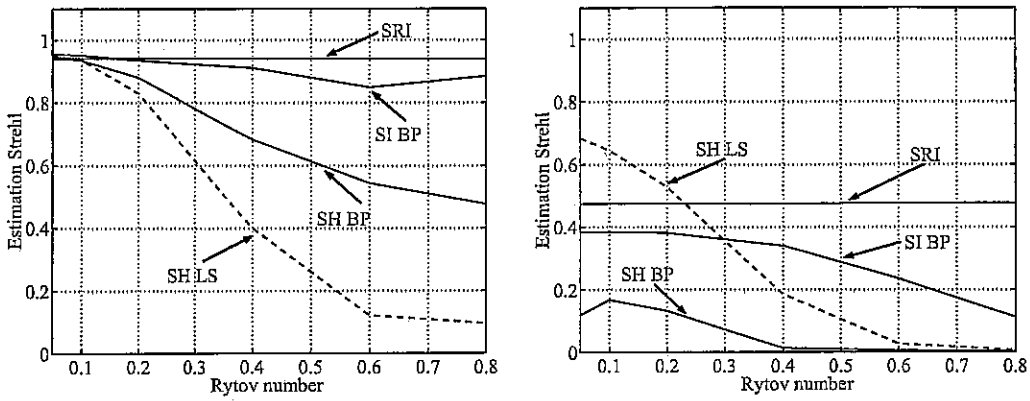

Figure 1. Simulation results comparing the wave front estimation accuracy as a function of Rytov number for a Shack-Hartmann WFS with a least-squares reconstructor (SH LS) or a branch point reconstructor (SH BP), a shearing interferometer WFS with a branch point reconstructor (SI BP), and a SRI WFS. The estimation Strehl is the normalized inner-product of the estimated wave front with the true wave front. Figure (a) shows the performance when the atmospheric coherence length r_0 is 4 times larger than the subaperture size d. Figure (b) shows the performance when $r_0 = d$. The graphs show that the accuracy of the SRI WFS is immune to scintillation and that it performs significantly better than the other WFSs is strong scintillation.

2.1. Design and Operation

The SRI WFS is based on a phase-shifting, point diffraction interferometer.[13] It can be implemented in a variety of configurations, three of which are shown in figure 2. In the configurations shown, the incoming complex field $U_0(\vec{r},t)$ is split into a signal beam $U_s(\vec{r},t)$ and a reference beam $U_r(\vec{r},t)$ using a variable beam splitter. In this notation $\vec{r}$ is a spatial position vector and t is time. The parameter f denotes the fraction of the input power transmitted to the signal beam. After splitting, the reference beam is focused onto a single mode fiber and optically amplified. The SRI laboratory demonstration being developed at the SOR will operate at a wavelength of $\lambda = 1.55\mu m$ due to the technology base of industry at this wavelength. Erbium doped fiber amplifiers (EDFAs) and semiconductor optical amplifiers (SOAs) are readily available for this wavelength. The tradeoffs between these amplifiers—gain, amplified spontaneous emission, optical path length, and cost—are discussed below.

The single mode fiber spatially filters the reference beam, outputting an amplified reference that is approximately Gaussian and that contains two components

$$U_{r,A}(t) = \sqrt{K\eta_c(t)}\, U_r(t) + U_{ASE}\,, \tag{1}$$

where K is the amplifier gain, η_c is the power coupling efficiency, and U_{ASE} is the complex field associated with the amplified spontaneous emission (ASE) produced by the amplifier. In writing this equation, it is assumed that standard optics are used to reshape the reference beam into a uniform, plane wave so that $U_{r,A}$ has no spatial dependence. The gain is generally reported in dB but is used as a gain factor in the above equation. Typical values for the gain range from 30-50 dB (K=1e3-1e5) for an EDFA and 15-25 dB (K=30-300) for a SOA. Typical values of the coupling efficiency range from less than 1e-3 for severely aberrated input beams (with no compensation from AO) to a maximum value near 0.8 when the input beam is a uniform, plane wave.[14] The ASE field is incoherent with respect to the signal and reference beams so its only effect is to introduce an overall background that reduces fringe visibility and contributes shot noise. For the small input powers of interest to the SOR project, saturation effects for the amplifier can be neglected and K and U_{ASE} can be considered constant.

After filtering and amplification, phase shifts of 0, $\pi/2$, π, and $3\pi/2$ are applied to the reference beam either spatially or temporally according to the configurations shown in figure 2. In figure 2(a), the reference and signal beams are each split into four beams with the necessary phase shifts applied to each of the reference beams using static optics. The reference and signal beams are then recombined to create four interference patterns on one or more detector arrays. In figure 2(b), the four phase shifts are applied to the reference beam temporally using a fiber-optic modulator. At each phase shift setting, one interference pattern is measured on the detector array. In

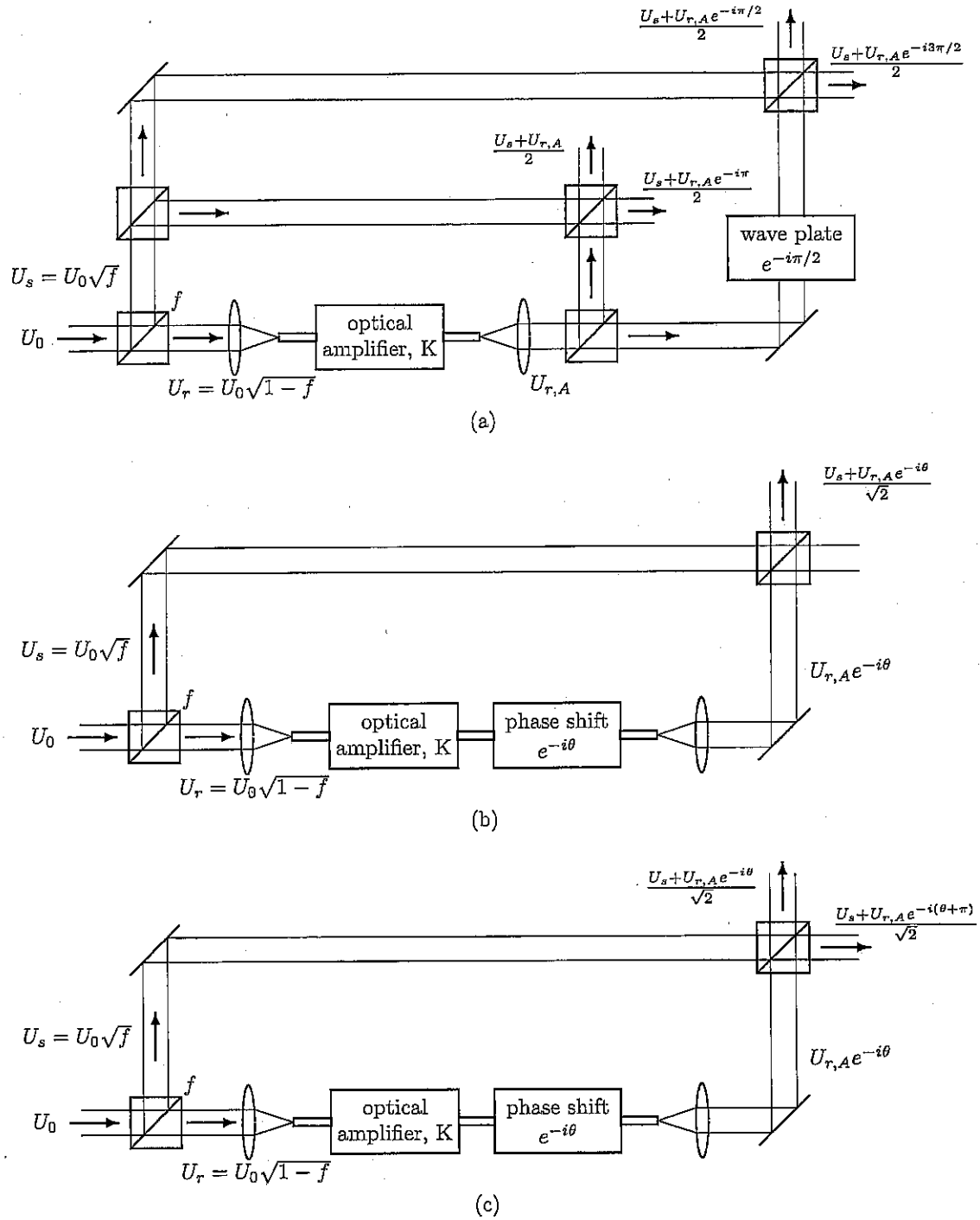

Figure 2. Possible configurations for the SRI WFS. Figure (a) shows a spatial phase-shifting configuration in which the interference patterns for all four phase shifts are measured simultaneously. Figure (b) shows a temporal phase-shifting configuration in which the measurements are collected one at a time over four consecutive integration cycles. Figure (c) shows a mixture of spatial and temporal phase shifting in which the four measurements are collected two at a time over two integration cycles. In all three configurations, 50% beam splitters are used for all but the first one. The first beam splitter is variable and is used to control the relative intensities of the signal and reference beams.

this configuration, half of the light is lost at the last beam splitter. However, it is possible to conserve this light by combining the spatial and temporal phase-shifting schemes as shown in figure 2(c). In this configuration, the two interference patterns created by the last beam splitter are imaged onto one or two detector arrays. These two patterns will differ by a π phase shift. Zero and $\pi/2$ phase shifts are then applied with the fiber optic modulator on alternating frames to create the four required interference patterns. These three configurations are parameterized by the variable N_{split}, which indicates the number of beams into which the signal and reference beams are divided. For the first configuration $N_{split} = 4$, while for the other two configurations $N_{split} = 2$.

In the absence of noise, the intensity measured in the k'th subaperture (i.e., camera pixel) is given by

$$I_n(\vec{r}_k, t) = \frac{1}{N_{split}} \int_t^{t+T_{int}} d\tau \int_{\mathcal{A}_k} d\vec{r} \left| U_s(\vec{r}, \tau) + U_{r,A}(\tau) e^{-i(n-1)\pi/2} \right|^2 , \tag{2}$$

where $\vec{r}_k$ is the location of the subaperture center, T_{int} is the camera integration time, $\mathcal{A}_k$ describes the spatial extent of the k'th subaperture, $(n-1)\pi/2$ is the phase shift applied to the reference beam, and $n = 1, 2, 3, 4$. By using equation 1, defining $U_s(\vec{r}, t) = A_s(\vec{r}, t) \exp(i\phi_s(\vec{r}, t))$, and assigning the reference to have zero phase (i.e., $U_r(t) = A_r(t)$), this expression becomes

$$\begin{aligned} I_n(\vec{r}_k, t) &= \frac{1}{N_{split}} \int_t^{t+T_{int}} d\tau \int_{\mathcal{A}_k} d\vec{r} \Big[A_s^2(\vec{r}, t) + K\eta_c(t) A_r^2(t) + |U_{ASE}|^2 \\ &\qquad + 2\sqrt{K\eta_c(t)} A_r(t) A_s(\vec{r}, t) \cos\left(\phi_s(\vec{r}, t) + (n-1)\pi/2\right) \Big] . \end{aligned} \tag{3}$$

These intensities are used to estimate the incident wave front in the k'th subaperture using the relation

$$\begin{aligned} \hat{U}_0(\vec{r}_k, t) &= \left[I_1(\vec{r}_k, t) - I_3(\vec{r}_k, t) \right] + i \left[I_4(\vec{r}_k, t) - I_2(\vec{r}_k, t) \right] \\ &= \frac{4}{N_{split}} \int_t^{t+T_{int}} d\tau \int_{\mathcal{A}_k} d\vec{r} \sqrt{K\eta_c(t)} A_r(t) A_s(\vec{r}, t) \left[\cos\left(\phi_s(\vec{r}, t)\right) + i \sin\left(\phi_s(\vec{r}, t)\right) \right] \\ &= \frac{4}{N_{split}} \int_t^{t+T_{int}} d\tau \int_{\mathcal{A}_k} d\vec{r} \sqrt{K\eta_c(t)}\, A_r(t)\, U_s(\vec{r}, t) . \end{aligned} \tag{4}$$

If the subaperture area is small enough so that the field can be considered constant within it and if the measurements are fast enough so that none of the parameters change significantly over the measurement period, then the noise-free, wave front estimate $\hat{U}_0$ is directly proportional to the field within the subaperture

$$\hat{U}_0(\vec{r}_k, t) = \frac{4}{N_{split}} T_{int} \mathcal{A}_k \sqrt{K\eta_c(t)}\, A_r(t)\, U_s(\vec{r}_k, t) . \tag{5}$$

2.2. Amplified Spontaneous Emission

One of the primary issues which limits the performance of the SRI WFS is ASE. ASE is a result of pumping the gain medium of the optical amplifier and is present even when no light is being coupled into the single mode fiber. As mentioned above, the ASE field is incoherent with respect to the signal and reference beams so it does not change the interference pattern between these two beam. However, it does introduce an overall background that reduces fringe visibility and contributes shot noise.

The ASE power is proportional to the amplifier gain K

$$P_{ASE} = (K-1)\, \mathit{NF} \left(\frac{\Delta\lambda\, c}{\lambda^2} \right) \left(\frac{h\, c}{\lambda} \right) , \tag{6}$$

where NF is the noise figure of the optical amplifier, λ is the nominal ASE wavelength, $\Delta\lambda$ is the width of the ASE wavelength spectrum, c is the speed of light, and h is Plank's constant. As with the amplifier gain, noise figure is typically reported in dB but is used as a gain factor in the above equation. EDFAs have noise figures as low as 3.1-3.5 dB (NF=2.05-2.25, 3 dB or NF=2 is the theoretical limit) while SOAs tend to have noise figures around 9-10 dB (NF=8-10). The spectral width, and hence the power, of the ASE is typically controlled with a narrow bandpass filter. For the small input powers of interest to the SOR project, saturation effects for the amplifier can be neglected

and K, $\mathcal{NF}$, and P_{ASE} can be considered constant. For analysis, it is convenient to define a gain-independent, threshold ASE irradiance in units of photons/m^2/s .

$$I_{ASET} = |U_{ASET}|^2 = \frac{1}{A}\,\mathcal{NF}\left(\frac{\Delta\lambda c}{\lambda^2}\right) , \tag{7}$$

where $U_{ASET} = U_{ASE}/\sqrt{K-1}$ and A is the area over which the reference beam $U_{r,A}$ is distributed. It is assumed that standard optics are used to reshape the approximately Gaussian reference beam into a uniform, plane wave with area A.

2.3. Noise Performance Analysis

In practice, the calculation in equation 5 is corrupted by noise, specifically shot noise, read noise, and quantization noise. When noise is present in the measurement, the wave front estimate is given by

$$\begin{aligned}\hat{U}_N(\vec{r}_k,t) \;=\; & \frac{4\mathcal{ND}\eta_{qe}}{N_{split}}\,T_{int}\mathcal{A}_k\sqrt{K\eta_c(t)}\,A_r(t)\,U_s(\vec{r}_k,t) \\ & + \sum_{p=1,3}[n_{s,p}(\vec{r}_k,t) + n_{r,p} + n_{q,p}] + i\sum_{p=2,4}[n_{s,p}(\vec{r}_k,t) + n_{r,p} + n_{q,p}] \; .\end{aligned} \tag{8}$$

where $n_{s,p}$, $n_{r,p}$, and $n_{q,p}$ are the shot, read, and quantization noise for measurement p, respectively. The effect of these noise sources on the accuracy of the wave front estimate is analyzed in this section. $\mathcal{ND}$ is the power attenuation factor of a neutral density filter placed in front of each camera to avoid saturation and η_{qe} is the quantum efficiency of the cameras.

There are three sources of shot noise—the signal beam, the reference beam, and ASE. For the k'th subaperture, the variance of $n_{s,p}$, averaged over the four measurements, is given by

$$\sigma^2_{shot}(\vec{r}_k,t) = \frac{\mathcal{ND}\eta_{qe}}{N_{split}}\left[I_s(\vec{r}_k,t) + K\eta_c I_r(t) + (K-1)I_{ASE}\right] , \tag{9}$$

where

$$I_s(\vec{r}_k,t) = T_{int}\;\mathcal{A}_k\;A_s^2(\vec{r},t), \qquad I_r(t) = T_{int}\;\mathcal{A}_k\;A_r^2(t), \qquad \text{and} \qquad I_{ASE} = T_{int}\;\mathcal{A}_k\;I_{ASET} \tag{10}$$

are the subaperture intensities for the signal, reference, and ASE beams, respectively.

Each camera used to measure the four interference patterns has an associated pixel read noise variance σ^2_{rd} and a quantization error σ^2_q. Given a maximum well depth W, a corresponding maximum number of output counts N_{count}, and assuming a uniform distribution for the quantization error and a linear detector, the variance of the quantization noise for a single camera pixel is given by

$$\sigma^2_q = \frac{1}{12}\left(\frac{W}{N_{count}}\right)^2 . \tag{11}$$

In order to avoid saturation of the well, a neutral density filter, with an attenuation factor of $\mathcal{ND}$, is placed in front of the camera.

The loss in wave front estimation accuracy due to noise over N_{sub} subapertures is characterized using the estimation Strehl

$$\mathcal{S}_N\left[\hat{U}_0(\vec{r},t),\hat{U}_N(\vec{r},t)\right] = \frac{\left\langle\left|\sum_{k=1}^{N_{sub}}\hat{U}_0(\vec{r}_k,t)\hat{U}_N^*(\vec{r}_k,t)\right|^2\right\rangle}{\left\langle\sum_{k=1}^{N_{sub}}\hat{U}_0(\vec{r}_k,t)\hat{U}_0^*(\vec{r}_k,t)\right\rangle\left\langle\sum_{k'=1}^{N_{sub}}\hat{U}_N(\vec{r}'_k,t)\hat{U}_N^*(\vec{r}'_k,t)\right\rangle} , \tag{12}$$

where '$\langle\ \rangle$' is the expectation operator and '*' denotes the complex conjugate. To reduce this equation three assumptions are made: 1) the noise in the subapertures is uncorrelated, 2) the signal beam has a uniform irradiance profile ($I_s(\vec{r},t) = I_s(t)$), and 3) N_{sub} is large ($N_{sub} \gg 1$). With these assumptions, equation 12 becomes

$$\mathcal{S}_N = \frac{\left(4\mathcal{ND}\eta_{qe}/N_{split}\right)^2 K\eta_c I_r(t) I_s(t)}{\left(4\mathcal{ND}\eta_{qe}/N_{split}\right)^2 K\eta_c I_r(t) I_s(t) + 4\sigma^2_{rd} + 4\sigma^2_q + 4\sigma^2_{shot}(t)} . \tag{13}$$

This expression can be rewritten in terms of a modulation signal to noise ratio SNR_M

$$S_N = \frac{1}{1 + \frac{1}{SNR_M^2}}, \tag{14}$$

where

$$SNR_M = \sqrt{\frac{4(\mathcal{ND}\eta_{qe}/N_{split})^2 K \eta_c I_r(t) I_s(t)}{\sigma_{rd}^2 + \sigma_q^2 + \sigma_{shot}^2(t)}}. \tag{15}$$

The numerator of this expression is the measured modulation depth of the interference fringes and the denominator is the measurement noise. At this point, it is convenient to define an input power parameter β that characterizes the amount of light available to the SRI WFS from the incident beam

$$\beta = \left(\frac{1}{A}\int d\vec{r}\,|U_0(\vec{r},t)|^2\right)/I_{ASET} = (I_s + I_r)/I_{ASE}. \tag{16}$$

Using this parameter, the beam splitter parameter f, and the expression for the shot noise, SNR_M can be expressed in terms of the threshold subaperture ASE intensity, I_{ASE},

$$SNR_M = \sqrt{\frac{4(\mathcal{ND}\eta_{qe}/N_{split})^2 K \eta_c f(1-f)\beta^2 I_{ASE}^2}{\sigma_{rd}^2 + \sigma_q^2 + (\mathcal{ND}\eta_{qe}/N_{split})\left[f\beta + K\eta_c(1-f)\beta + (K-1)\right] I_{ASE}}}. \tag{17}$$

2.4. Sample Noise Performance Evaluation

The design and analysis of the SRI WFS proceeds by assuming we are given optical amplifier characteristics (NF, λ, and $\Delta\lambda$), camera characteristics (W, N_{count}, η_{qe}, and σ_{rd}^2), and a total input power characterized by β. With this information, we select the beam splitter parameter f, the amplifier gain K, and $\mathcal{ND}$ to maximize performance of the SRI over a range of values for the coupling efficiency η_c. Two performance metrics will be used. The first metric is an indicator of the ability to close an AO loop with a SRI WFS. Experience with wave optical simulations has shown that, if the average value of SNR_M is greater than 1, an AO loop can be closed using the measurements from an SRI. Therefore, the first performance metric, η_{min}, is defined as the minimum value of η_c for which $SNR_M > 1$. The second performance metric is the steady state modulation signal to noise ratio, $\overline{SNR}_M$, defined as the average value of SNR_M over the interval $\eta_c \in [0.1, 0.8]$. This metric is an indicator of the steady state performance of the SRI WFS once the AO loop is closed. The averaging of this metric over a range of η_c is performed because it is assumed that in steady-state, closed-loop operation η_c will oscillate but it should remain within the range $0.1 - 0.8$.

In the remainder of this section, the noise sensitivity of the SRI WFS is evaluated for an example application being considered as part of the SRI laboratory demonstration project at the SOR. In this example, the phase-shifting configuration shown in figure 2(c) is evaluated using either an EDFA or an SOA as the optical amplifier. In this configuration, phase shifts of 0 and $\pi/2$ are applied to the reference beam on alternating camera integration cycles by the fiber optic modulator and the four interference patterns are measured over two consecutive camera integrations. The SRI will be used to control a single DM with 24 actuator spacing across the pupil of the AO system—corresponding to 25 actuators across the pupil. The SRI is aligned with the DM such that an actuator is at the center of each WFS subaperture. For each subaperture the SRI will be used to produce a phase measurement that is applied to the DM actuator for that subaperture. The integration period is set to 100 μ sec, corresponding to a frame rate of 10 kHz. (Due to cost, the SOR laboratory demonstration will use video rate cameras. However, the turbulence simulator system being constructed allows full control of the strength and speed of the turbulence over a wide range of conditions, making it possible to simulate a 10 kHz system by appropriately choosing the speed of the turbulence.) The other camera and amplifier characteristics are summarized in table 1. The parameters in the table were chosen based on a review of commercial, off-the-shelf products.

As mentioned in the previous section, a neutral density filter is placed in front of each camera in order to avoid saturation. Using this filter, we impose the constraint that, assuming unit coupling ($\eta_c = 1$), the expected peak signal level on the detector is less than 3/4 of the subaperture well capacity W. This rule of thumb generally should be sufficient to ensure saturation is avoided even in strong scintillation conditions.

Upon investigation, it was discovered that, with the system parameters listed in table 1, if a single camera pixel was used for each subaperture, the modulation signal to noise ratio was unduly limited by the saturation constraint.

Table 1. System parameters for the example noise evaluation.

parameter	value	parameter	value
RMS pixel read noise σ_{rd}	1200 e^-	integration period T_{int}	100 μ s
pixel well depth W	3.5e6 e^-	limits on the value of f	[0.01,0.99]
number of counts in well N_{count}	16384	EDFA noise figure NF_{EDFA}	3.1 dB
detector quantum efficiency η_{qe}	0.7	SOA noise figure NF_{SOA}	9 dB
number of pixels across the pupil	193	wavelength λ	1.55 μm
number of pixels per binned subaperture	8 × 8	width of spectral filter $\Delta\lambda$	2 nm
number of subapertures across the pupil	25		

It was found that any increase of the amplifier gain lead to a reduction in SNR_M. In order to circumvent this problem, and create conditions in which a meaningful demonstration can be carried out, the subaperture well size was artificially increased by binning the measurements from many pixels. An 8 × 8 block of pixels was assigned to each subaperture so that there were 193 pixels across the pupil (the edge subapertures are only partially illuminated). In addition to increasing the effective well size, an inspection of the derivation of equation 17 shows that binning also increases SNR_M by roughly the square root of the number of binned subapertures, or by a factor of 8 in this case.

In the analysis and design procedure a range of values for the input power, as characterized by β, and the amplifier gain K are considered. This approach is reasonable since β and K can be measured *a priori*. For each (β, K) pair, the optimal values of the beam splitter parameter f that minimize η_{min} and maximize $\overline{SNR}_M$ are determined. For each of these optimizations the values of ND which satisfy the saturation constraint are also recorded. The end result of this process is a set of curves for different values of β that indicate the minimum coupling efficiency to close the AO loop as well as the average steady state modulation signal to noise ratio.

The analysis procedure was carried out for an SRI system using either an EDFA or a SOA as the optical amplifier. The results for these two systems are compared in figure 3. The graphs of $\overline{SNR}_M$ indicate three gain regions of operation. In the low gain region $\overline{SNR}_M \propto \sqrt{K}$. The cause of this behavior can be determined by examining the equation for SNR_M. Assuming f is roughly constant in this region (a condition illustrated in the graphs) and assuming the camera read and quantization noise is much larger than the shot noise, equation 17 becomes

$$SNR_M \approx \sqrt{\frac{4(ND\eta_{qe}/N_{split})^2 K\eta_c f(1-f)\beta^2 I_{ASE}^2}{\sigma_{rd}^2 + \sigma_q^2}}, \tag{18}$$

and the modulation signal to noise ratio is clearly seen to be proportional to $\sqrt{K}$. In this region, performance is dominate by camera read and quantization noise and performance can be improved by increasing the gain. In the intermediate gain region performance is dominated by shot noise. Consideration of this noise scenario reduces equation 17 to

$$SNR_M \approx \sqrt{\frac{4(ND\eta_{qe}/N_{split})K\eta_c f(1-f)\beta^2 I_{ASE}^2}{[f\beta + K\eta_c(1-f)\beta + (K-1)]\, I_{ASE}}}. \tag{19}$$

In this expression, the numerator is proportional to K and the denominator is roughly proportional to K (particularly for values of $K \gg 1$), so gain does not effect performance very much. This condition is illustrated by the relatively flat portions of the curves for $\overline{SNR}_M$. In the high gain region $\overline{SNR}_M \propto \sqrt{1/K}$. The cause of this behavior can be understood by examining equation 19 in conjunction with the graphs in figures 3(e) and (f). As shown in the graphs, a neutral density filter must be used to avoid saturation of the camera and the amount of attenuation is proportional to $1/K$. In this situation, equation 19 becomes

$$SNR_M \propto \sqrt{\frac{4(\eta_{qe}/N_{split})\eta_c f(1-f)\beta^2 I_{ASE}^2}{[f\beta + K\eta_c(1-f)\beta + (K-1)]\, I_{ASE}}} \tag{20}$$

and the modulation signal to noise ratio is seen to go roughly as $\sqrt{1/K}$. In this region, performance is dominate by the saturation constraint and increasing gain causes a degradation of performance. This behavior can be further understood by noting that equation 20 is similar to an expression for the fringe visibility of the measured interference

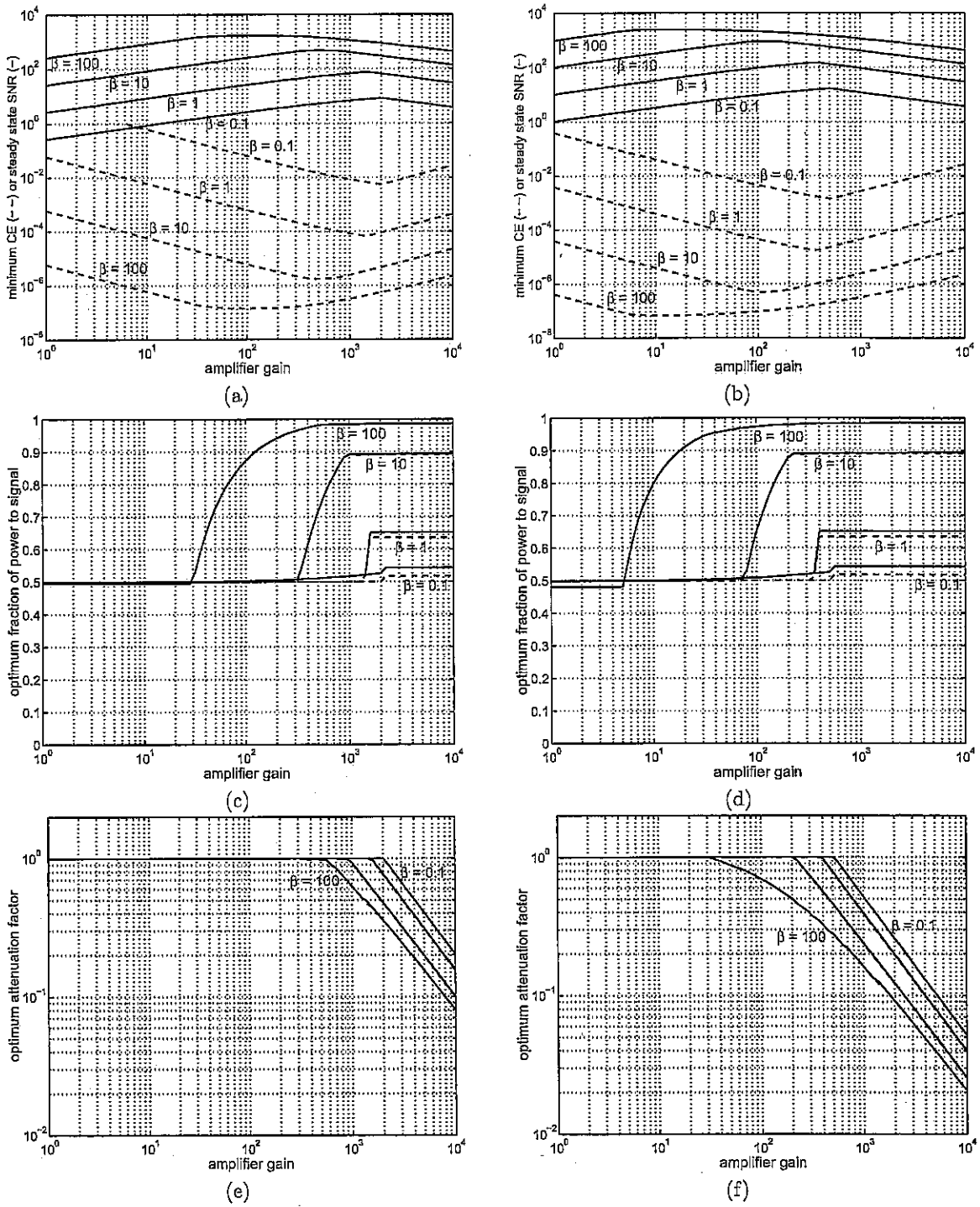

Figure 3. Performance evaluation for a SRI WFS with an EDFA (left column) and a SOA (right column) for different values of β as a function of the amplifier gain. Figures (a) and (b) illustrate the steady state SNR_M (solid lines) and η_{min} (dashed lines). Figures (c) and (d) show the optimal value for f that optimizes either the steady state SNR_M (solid lines) or η_{min} (dashed lines). Figures (e) and (f) show the value for ND associated with optimizing either the steady state SNR_M (solid lines) or η_{min} (dashed lines). Several of the solid and dashed curve pairs overlap in the four bottom figures.

patterns. In the high gain region, increasing the gain results in a decrease in fringe visibility so that estimation of the signal wave front is less accurate.

All three gain regions of operation are evident in the graphs of the steady state modulation signal to noise ratio shown in figures 3(a) and (b). These same regions are also seen in the graphs of the minimum coupling efficiency but the trends for for these regions are $\eta_c \propto 1/K$, $\eta_c \propto 1$, and $\eta_c \propto K$. This behavior is understood by noting that $SNR_M \propto \sqrt{\eta_c}$.

It is noteworthy that the optimal value of f and the value of ND used to satisfy the saturation constraint are about the same whether the goal is to minimize η_{min} or maximize $\overline{SNR}_M$. This result is good news and indicates that a system designed to maximize steady state performance (i.e., maximize $\overline{SNR}_M$) will also maximize robustness (i.e., minimize η_{min}), or vice versa.

2.5. Optical Amplifier Comparison

The selection of the optical amplifier is an important decision which effects many aspects of the SRI WFS design. When choosing between an EDFA and a SOA there are many factors to consider. Regarding gain, commercial EDFAs typically offer gains as high as 30-50 dB while competing SOAs typically have gains between 15-25 dB. However, there is a down side associated with gain. As shown in equation 6, the ASE power is proportional to gain, so higher gains produce higher ASE background levels and reduce the fringe visibility of the interference patterns. In addition, the example presented in the last section shows that, as gain increases, a point is reached at which attenuation of the interference patterns is required so as not to saturate the camera. In this regime, increasing the gain causes a degradation in performance. A major lesson learned from the example is that the gain must be high enough to overcome camera read and quantization noise but not so much that a neutral density filter is required to avoid camera saturation.

Noise figure is another property of optical amplifiers that must be considered. As shown in equation 6, besides being proportional to gain, the ASE power is proportional to the noise figure. The noise figure of an EDFA is typically smaller than a SOA—as low as 3.1 dB for an EDFA compared to 9-10 dB for a SOA. As with gain, higher noise figures produce higher ASE background levels. On the other hand, lower noise figures allow the SRI to work with lower light levels. Consider the example in the last section. For the range of values of β evaluated, figures 3(a) and (b) indicate that a gain of about 200 (23 dB) can be considered near optimal for both the EDFA and the SOA. For this gain, values of β greater than 1 can be expected to provide good performance (i.e., $\overline{SNR}_M \gtrsim 100$). From the graphs it appears that for equal values of β the performance of the SOA is better than for the EDFA. However, this comparison is somewhat misleading due to the difference in NF. For the EDFA the noise figure is 3.1 dB, corresponding to an ASE power of $P_{ASE} = 0.13$ μW. In comparison, for the SOA, the noise figure is 9 dB, which corresponds to an ASE power of $P_{ASE} = 0.51$ μW. So for equal values of β the EDFA is operating with 4 times less light than the SOA.

Beyond gain and noise figure, the optical path length and cost of the optical amplifier may be important considerations. EDFAs have higher gains and lower noise figures compared to SOAs but they also introduce longer optical paths and cost several times as much. An EDFA with a gain of 40 dB typically contains a few tens of meters of fiber. The difficulty with this length of fiber is that the coherence length of the incident wave front will most likely be measured in centimeters or less. In order to obtain interference fringes at the camera, the optical path of the signal beam U_s must be extended to account for the optical path introduced into the reference beam U_r by the amplifier. For some applications, this situation is impractical. On the other hand, a SOA introduces only a few meters of optical path, most of which is due to the fiber interface. Finally, regarding cost, EDFAs tend to be 2-3 times as expensive as SOAs. The cost of an EDFA is on the order of \$15 thousand while the cost of a SOA is around \$5 thousand.

2.6. Tradeoffs Between Spatial and Temporal Phase Shifting

As shown in figure 2, there are a number of ways in which the phase shifting for the SRI WFS can be accomplished. Phase shifting can be done spatially so that all four measurements are captured simultaneously or it can be done temporally so that the measurements are captured in a sequence of four time steps. Alternatively, a combination of spatial and temporal phase shifting can be used. While this last option was considered for the example presented above, the effects of temporal phase shifting on performance were ignored in the calculations.

The issue of how to implement the phase shifting warrants some discussion of the tradeoffs involved. For spatial phase shifting, the incident wave front is split into several beams which are recombined on different detector arrays

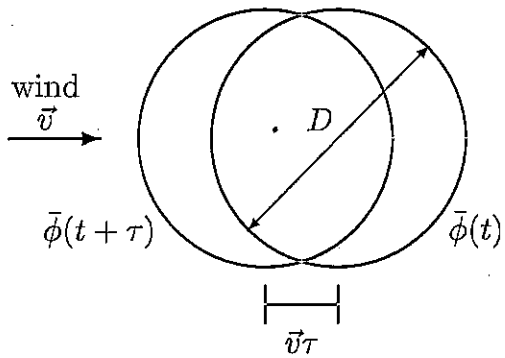

Figure 4. A plane wave of diameter D propagating through a layer of atmospheric turbulence. At time t the beam is indicated by the circle on the right. A time τ later, the turbulence has moved and the beam is effectively shifted a distance $v\tau$ to the left.

(or different portions of the same array). While this approach ensures the same wave front is used for all four of the interference measurements it also presents a few problems. It either requires multiple cameras, possible making cost a concern, or all four interference patterns must be placed on the same camera. In either scenario, co-aligning the wave fronts on the cameras and maintaining the proper relative phase shifts between the different interference patterns is non-trivial, making the hardware requirements more complex. In addition, the calibration of the different cameras must be accurately known so the gain and bias variations can be corrected before the different measurements are combined to reconstruct the wave front. Lastly, static, non-common path aberrations in the different beams corrupt the wave front estimation process.

For temporal phase shifting, the requirements on optical alignment and camera calibration are drastically simplified since only a single detector array is used. For each WFS subaperture, the same camera pixels are used for all four measurements so there are no co-alignment issues or concerns about non-common path aberrations. In addition, the same gain and bias is present in all four measurements so the camera calibration is not as important. Furthermore, if only a single camera is available, temporal phase shifting provides higher resolution. If the camera has $N \times N$ pixels, temporal phase shifting can operate with $N \times N$ subapertures. On the other hand, placing all four images on the camera for spatial phase shifting only allows an $\frac{N}{2} \times \frac{N}{2}$ grid of subapertures.

While temporal phase shifting offers several advantages over spatial phase shifting, the major concern with its implementation is that atmospheric turbulence is dynamic. The field within each subaperture changes with time and, thus, will not be constant for all of the interference measurements. In the remainder of this section, a first-order parameterization of the magnitude of the phase change within a subaperture with time is developed. The magnitude of the change in the field amplitude is dealt with in reference [12] and the reader is directed there for details. However, it is assumed that if the changes in the wave front phase are small the corresponding changes in the wave front amplitude will also be small.

The derivation begins by considering a uniform, plane wave propagating through a thin layer of atmospheric turbulence moving at a velocity $\vec{v}$. A small portion of the wave front with diameter D is considered as shown in figure 4. We assume this portion corresponds to either the full aperture of the AO system or a single subaperture of the SRI WFS. (A subaperture is generally square but in this analysis it is assumed to be a circle.) At time t the average phase across the beam is defined as

$$\bar{\phi}(t) = \int d\vec{\rho}\, \phi\left(\frac{D}{2}\vec{\rho}, t\right) W(\vec{\rho}), \tag{21}$$

where $\phi(\vec{r}, t)$ is the phase at position $\vec{r}$ and time t and the windowing function $W(\vec{r})$ is defined as

$$W(\vec{\rho}) = \begin{cases} 1/\pi & |\vec{\rho}| \leq 1 \\ 0 & \text{else} \end{cases} \tag{22}$$

A time τ later the wind has moved the phase screen a distance $\vec{v}\tau$. Assuming frozen flow, the average phase across

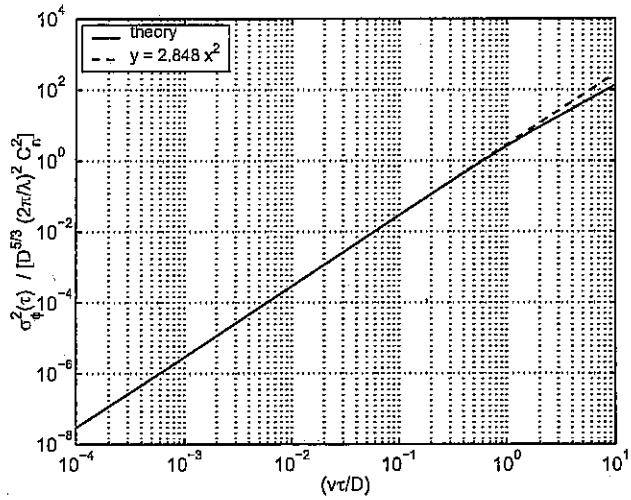

Figure 5. The variance of the change in the average phase of a wave front propagating through a thin layer of atmospheric turbulence.

the beam is given by

$$\bar{\phi}(t+\tau) = \int d\vec{\rho}\; \phi\left(\frac{D}{2}\vec{\rho}, t+\tau\right) W(\vec{\rho}) = \int d\vec{\rho}\; \phi\left(\frac{D}{2}\vec{\rho} - \vec{v}\tau, t\right) W(\vec{\rho}). \tag{23}$$

The variance of the change in the average phase is given by

$$\sigma_{\bar{\phi}}^2(\tau) = \left\langle \left(\bar{\phi}(t) - \bar{\phi}(t+\tau)\right)^2 \right\rangle. \tag{24}$$

Following the analysis presented by Noll and applying Parseval's theorem,[15] the variance can be expressed as

$$\sigma_{\bar{\phi}}^2(\tau) = \frac{16}{\pi D^2} \int_0^\infty d\kappa\; \kappa^{-1} \Phi\left(\frac{2}{D}\kappa\right) J_1^2(2\pi\kappa) \left[1 - J_0\left(4\pi \frac{v\tau}{D}\kappa\right)\right], \tag{25}$$

where $\Phi(x)$ is the power spectral density of the turbulence, $J_n(x)$ is the n'th order Bessel function of the first kind, and $v = |\vec{v}|$. Assuming Kolmogorov turbulence statistics and substituting $x = 2\pi\kappa$, this expression becomes

$$\sigma_{\bar{\phi}}^2(\tau) = 3.282\; D^{5/3} \left(\frac{2\pi}{\lambda}\right)^2 C_n^2 \int_0^\infty dx\; x^{-14/3} J_1^2(x) \left[1 - J_0\left(\frac{2v\tau}{D}x\right)\right], \tag{26}$$

where C_n^2 is the index of refraction structure constant.

A numerical evaluation of the variance is shown in figure 5. As shown in the graph, for small values of $v\tau/D$ the variance is closely approximated by

$$\sigma_{\bar{\phi}}^2(\tau) = 2.848 (v\tau)^2\; D^{-1/3} \left(\frac{2\pi}{\lambda}\right)^2 C_n^2. \tag{27}$$

This variance is the contribution from a single turbulence layer. In order to determine the cumulative effect over an extended path, we must integrate over the path

$$\sigma_{\bar{\phi}}^2(\tau) = \int_{\mathcal{L}} dz\; \sigma_{\bar{\phi}}^2(z, \tau), \tag{28}$$

where $\mathcal{L}$ indicates the extent of the propagation path. By substituting equation 27 into the integrand of this

expression, the cumulative average phase variance is found

$$\begin{aligned}\sigma_{\phi}^2(\tau) &= 2.848\tau^2\, D^{-1/3}\left(\frac{2\pi}{\lambda}\right)^2 \int_{\mathcal{L}} dz\, C_n^2(z) v^2(z) \\ &= 1026\,\tau^2\left[(0.331)^2 D^{-1/3}\lambda^{-2}\int_{\mathcal{L}} dz\, C_n^2(z) v^2(z)\right] \\ &= 1026\,\tau^2 f_T^2 \end{aligned} \tag{29}$$

The last step is accomplished by noting that the term in brackets is the square of the Tyler frequency f_T.[16] The effect of the changing phase on each interference measurement for a subaperture is found by combining the variations in the subaperture and over the full aperture (i.e., in the reference). Assuming the full aperture is significantly larger than a subaperture, the phase variations can be considered uncorrelated and the measurement phase variance is

$$\begin{aligned}\sigma_{meas}^2 &= 1026\,\tau^2\left(f_{T,sub}^2 + f_{T,full}^2\right) \\ &= 1026\left[1+\left(\frac{D_{sub}}{D_{full}}\right)^{1/3}\right]\tau^2 f_{T,sub}^2 \end{aligned} \tag{30}$$

where the subscripts *sub* and *full* denote parameters for a subaperture and the full aperture, respectively.

The expression for σ_{meas}^2 can be used to estimate the loss in wave front estimation accuracy caused by temporal phase shifting. Consider the scenario in which the four interference measurements are collected sequentially at a sample rate of f_s and they are used to estimate the field at the average measurement time (i.e., the time half-way between the second and third measurements). In this case $\tau = \frac{3}{2f_s}$ and the average phase variance is given by

$$\sigma_{meas}^2 = 2308\left[1+\left(\frac{D_{sub}}{D_{full}}\right)^{1/3}\right]\left(\frac{f_{T,sub}}{f_s}\right)^2. \tag{31}$$

Using a standard four-bin algorithm for a phase-shifting interferometer (as in equation 5) and assuming that the average phase variance is small and that the phase errors in the measurements are uncorrelated, the error in the phase of the field estimate within each subaperture is given by[17]

$$\begin{aligned}\varepsilon^2 &= \frac{\sigma_{meas}^2}{4} + \frac{\sigma_{meas}^2}{4}\cos^2(2\theta) + \frac{3\sigma_{meas}^4}{64}\sin^2(2\theta) \\ &\leq \frac{\sigma_{meas}^2}{2} \\ &\leq 1154\left[1+\left(\frac{D_{sub}}{D_{full}}\right)^{1/3}\right]\left(\frac{f_{T,sub}}{f_s}\right)^2. \end{aligned} \tag{32}$$

where θ is the subaperture phase at the average measurement time. The second step assumes $\sigma_{meas}^2 \leq 4/\sqrt{3}$, which is satisfied under the assumption that the average phase variance is small. For the error in the estimate to be small, say $\varepsilon^2 < 0.1$, the SRI sample rate must be 100-150 times faster than the Tyler frequency.

Assuming the phase estimation error is uniform over the wave front, the loss in estimation Strehl due to temporal phase shifting can be approximated by

$$\mathcal{S}_\tau = e^{-\varepsilon^2} \geq \exp\left\{-1154\left[1+\left(\frac{D_{sub}}{D_{full}}\right)^{1/3}\right]\left(\frac{f_{T,sub}}{f_s}\right)^2\right\} \tag{33}$$

If $f_s > 100 f_{T,sub}$, the Strehl will be $\mathcal{S}_\tau \geq 0.9$, resulting in a negligible loss in performance. Sampling at this rate is not as difficult as it might appear because the Tyler frequency tends to be small, even in extreme scenarios. For example, consider a horizontal path propagation with a constant turbulence profile: C_n^2 = 1e-16, v = 50 m/s, and $\mathcal{L}$ = 50 km. For λ = 1.55 μm and a subaperture size of D_{sub} = 1 cm, the Tyler frequency is only 51 Hz and a sample frequency of 5-10 kHz should be sufficient to minimize the effects of temporal evolution of the wave front.

As mentioned above, this analysis only considers the effects of temporal evolution of the phase. Temporal evolution of the amplitude scintillation is ignored. A more complete analysis that combines these two effects needs to be completed. To end the discussion on temporal phase shifting, it should be noted that equation 33 is pessimistic due to the assumptions concerning the correlations of the various parameters.

3. CLOSING COMMENTS

The concept of a self-referencing interferometer wave front sensor with an amplified reference was presented and its noise performance was analyzed. The estimation accuracy of the SRI WFS was developed in terms of the modulation signal to noise ratio and, using this metric, it was shown that there are gain regions where the optical amplifier improves performance. However, it was also shown that there are regions where amplification degrades performance due to the presence of ASE and limits on the well size of the detector. The design of the SRI WFS must be performed carefully and, in general, the system should be designed so there is just enough gain to overcome camera read and quantization noise.

Numerical examples were presented comparing SRI performance for an EDFA and a SOA and various tradeoffs between the two amplifiers were discussed. The difference in the performance for the two amplifiers was not significant for the example application. The SOA introduces a shorter optical path, making it easier to implement, and, as such, it is preferred for use in the SOR laboratory demonstration, although it is likely that both devices will be tested.

Tradeoffs between spatial and temporal phase shifting were also discussed. Temporal phase shifting has several advantages over spatial phase shifting in regard to hardware complexity. However, the major drawback of temporal phase shifting is that the signal and reference fields are not constant over the measurement cycle. In terms of the average phase in a subaperture, the variations of the signal and reference fields were found to be proportional to the square of the Tyler frequency. As a rule of thumb, it was discovered that in order to keep the loss in estimation Strehl small, the SRI sample rate had to be more than 100 times faster than the Tyler frequency as seen by a subaperture.

REFERENCES

1. R. V. Shack and B. C. Platt, "Production and use of a lenticular Hartmann screen," J. Opt. Soc. Am. **61**, p. 656, 1971.
2. J. C. Wyant, "Use of an ac hetrodyne lateral shear interferometer with real-time wavefront correction systems," Appl. Opt. **14**, pp. 2622–2626, 1975.
3. D. L. Fried, "Least-squares fitting a wave-front distortion estimate to an array of phase difference measurements," J. Opt. Soc. Am. **67**, pp. 370–375, 1977.
4. R. H. Hudgin, "Wave-front reconstruction for compensated imaging," J. Opt. Soc. Am. **67**, pp. 375–378, 1977.
5. J. W. Hardy, *Adaptive Optics for Astronomical Telescopes*, Oxford U. Press, Oxford, 1998.
6. D. L. Fried and J. L. Vaughn, "Branch cuts in the phase function," Appl. Opt. **31**, pp. 2865–2882, 1992.
7. D. L. Fried, "Branch point problem in adaptive optics," J. Opt. Soc. Am. A **15**, pp. 2759–2768, 1998.
8. G. A. Tyler, "Reconstruction and assessment of the least-squares and slope discrepancy components of the phase," J. Opt. Soc. Am. A **17**, pp. 1828–1839, 2000.
9. J. D. Barchers, D. L. Fried, and D. J. Link, "Evaluation of the performance of Hartmann sensors in strong scintillation," Appl. Opt. **41**, pp. 1012–1021, 2002.
10. J. D. Barchers, D. L. Fried, and D. J. Link, "Evaluation of the performance of a shearing interferometer in strong scintillation in the absence of additive measurement noise," Appl. Opt. **41**, pp. 3674–3684, 2002.
11. D. L. Fried, "Adaptive optics wave function reconstruction and phase unwrapping when branch points are present," Optical Communications **200**, pp. 43–72, 2001.
12. J. D. Barchers and T. A. Rhoadarmer, "Evaluation of phase-shifting approaches for a point diffraction interferometer using the mutual coherence function," submitted to Appl. Opt. , 2001.
13. D. Malacara, *Optical Shop Testing*, Wiley, New York, 1992.
14. R. E. Wagner and W. J. Tomlinson, "Coupling efficiency of optics in single-mode fiber components," Appl. Opt. **21**, pp. 2671–2688, 1982.
15. R. J. Noll, "Zernike ploynomials and atmospheric turbulence," J. Opt. Soc. Am. **66**, pp. 207–211, 1976.
16. G. A. Tyler, "Bandwidth considerations for tracking through turbulence," J. Opt. Soc. Am. A **11**, pp. 358–367, 1994.
17. J. Schwider, "Phase shifting interferometry: reference phase error reduction," Appl. Opt. **28**, pp. 3889–3892, 1989.